



# Failure Analysis of a Fighter Jet Engine Compressor Blade Due to Foreign Object Damage and High-Cycle Fatigue

R. A. Marín · J. A. Escobar · J. Loboguerrero

Submitted: 26 April 2021 / Accepted: 25 June 2021 / Published online: 20 August 2021  
© ASM International 2021

**Abstract** Failures affecting the compressor components of jet engines are critical during their operation because they compromise flight reliability. Blades are one of the most critical components. They are subjected to high dynamic loads resulting from high rotational speeds and aerodynamic forces. A better understanding of the failure mechanisms that affect these components could provide a safer strategy in the operation and maintenance of jet engines. A fighter jet engine compressor blade failure was analyzed in this work. Mechanical, macroscopic, and microscopic observations were performed to identify deterioration of properties. SEM and EDS analysis were performed to assess crack propagation and to identify possible surface treatments performed during the manufacturing of the blade. The material of the blades was found to be martensitic stainless steel (AISI 403) and the blades presented an aluminized coating. A crack was identified to have started on the high-pressure side of the blade. Examination of the fractured surface indicates that the failure mechanism was fatigue. The presence of a dent on an edge of the fractured surface suggests that the cause of failure might have been foreign object damage (FOD) due to high-speed impact of one or more particles on the blade surface. The axial location of the failed blade inside the engine was such that the probability of suffering high-speed impact of hard particles ingested by the engine was not negligible. An analytical model is presented to determine if the stresses expected at the FOD location were high enough to cause fatigue failure of the blade.

**Keywords** Jet engine failure · High-cycle fatigue · Foreign object damage

## Introduction

Jet engine components operate in a particularly aggressive environment, where gases at high temperatures and dynamic mechanical loads promote creep-fatigue damage on compressor blades [1]. Continuous advances in the materials and manufacturing technology of blades have taken place over the years to produce structurally durable blades while reducing weight without compromising safety [2].

Compressor blades are at risk of failure from two sources: damage due to cyclic loading and damage caused by the high-velocity impact of ingested particles, causing FOD (Foreign Object Damage). Creep and fatigue, alone or combined, are among the main causes of failure in jet engines. FOD can generate small indentations that can become fatigue crack initiation sites. The propagation of these cracks can take place as a case of high-cycle fatigue (HCF) due to the blade vibrations and resonant airflow dynamics. This could severely decrease the lifespan of the blades [3].

This paper presents the failure analysis of a fractured blade from the second stage of the compressor in a fighter jet engine. A schematic cross-sectional view of the engine is shown in Fig. 1.

---

R. A. Marín (✉) · J. A. Escobar · J. Loboguerrero  
Departamento de Ingeniería Mecánica, Universidad de Los Andes, Carrera 1 Este # 19-A-40, Bogotá, Colombia  
e-mail: r.marin58@uniandes.edu.co

## Material Evidence

The failure took place at compressor stage #2. The following components from the second stage of the compressor of the failed engine were received as material evidence to determine the most probable cause of failure: 17 bent blades from the second stage of the compressor rotor, fragments of a fractured blade from the same source, and an undamaged reference blade (never put in service). The 17 bent blades were a subset of the 30 blades that are installed on the second stage of the engine compressor. The fractured blade was from that location too.

The 17 blades are shown in Fig. 2, mounted on the compressor rotor body. It is apparent that all the non-fractured blades suffered permanent bending deformation whereas the portion of the fractured blade attached to the rotor body remained straight.

The recovered portion of the fractured blade is shown in Fig. 3a, unmounted from the rotor. Fig. 3b shows the same element mounted on the rotor with an undamaged blade

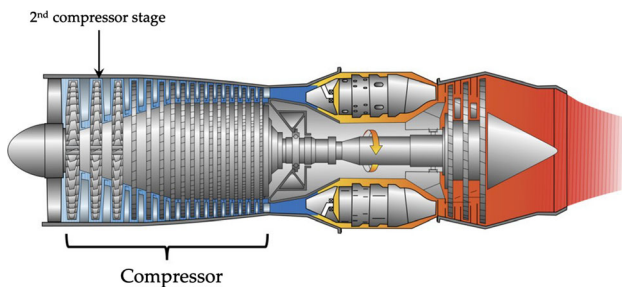


**Fig. 1** Schematic section view of the engine (Modified version of an illustration by Jeff Dahl)

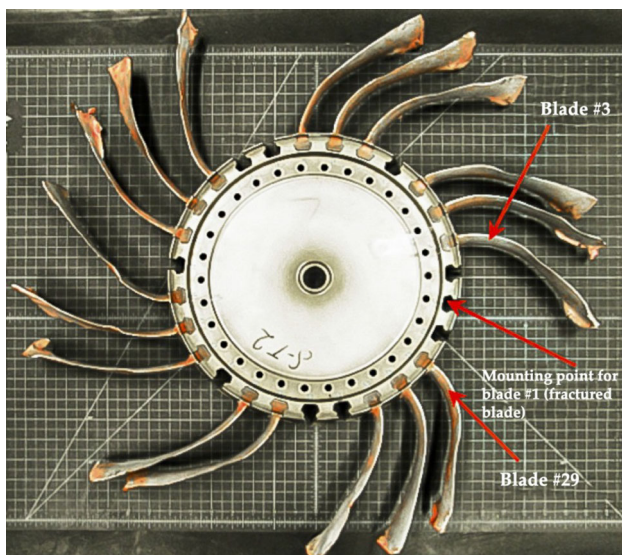


**Fig. 2** The compressor second stage with 17 bent blades. The fractured one was blade #1. Each square side is 0.5 in. long

superimposed to make more evident the location of the fracture.

## Material Characterization

### Blade Chemical Composition

To determine the chemical composition of the blades, two complementary analyses were carried out: Optical Emission Spectroscopy (OES) following the ASTM E1282 standard [4], with a Thermo ARL QuantaDesk spectrometer, and X-ray fluorescence (XRF) using a Rigaku ZSX Primus spectrometer.

Table 1 shows the results of the chemical composition analysis. The table also shows the chemical composition of a martensitic stainless steel AISI 403 from [5].

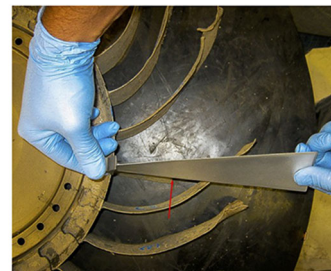
Thus, according to the chemical composition results, the fractured blade material belongs to the family of martensitic AISI 403 steels, which is commonly used in the manufacturing of compressor rotor blades of jet engines [6].

### Hardness Test

The hardness scale used for the measurements was Rockwell C (HRC, at a load of 150 kg), following standard



**(a)** Photograph of the portion of the fractured blade that remained attached to the rotor.



**(b)** An undamaged blade superimposed on the recovered portion of the fractured blade, mounted on the rotor.

**Fig. 3** Two views of the fractured blade

ASTM E18 [7]. The surface of the samples was cleaned and polished. To compare the mechanical properties of the material with those of AISI 403 steel, measurements were taken at different sections of the blades.

Hardness measurements were taken at the dovetail of blade No. 3 (28.3 HRC), blade No. 26 (27 HRC) and on the undamaged reference blade (29.2 HRC). Additional measurements were taken on the pressure side of blade No. 3 (27.3 HRC). Hardness results show that there is no significant difference between the sampled blades. This evidence shows that the normal operation of the engine did not cause changes in the mechanical properties for these components. Furthermore, these results are within the range commonly specified for a tempered AISI 403 steel (25–31 HRC) [8].

**Microhardness Test**

A microhardness test was conducted using the Vickers scale (HV, under a load of 500 g) according to the ASTM E384 standard [9]. The samples were metallographically prepared as shown in Fig. 4. Measurements were made from the trailing edge to the leading edge on the fractured blade (approximately 315 HV), on the reference blade (approximately 316 HV) and on blade No. 3 (approx-

**Table 1** Chemical composition of the fractured blade material (%.wt) from OES, XRF and EDS analyses

	C	Si	Mn	Cr	Ni	P	S	Fe
AISI 403	0.15	0.50	1.00	11.5–13.0	...	0.04	0.03	Balance
OES	0.15	0.32	0.40	11.39	0.19	0.02	0.01	Balance
XRF	...	0.13	0.12	13.82	0.16	0.01	0.01	Balance

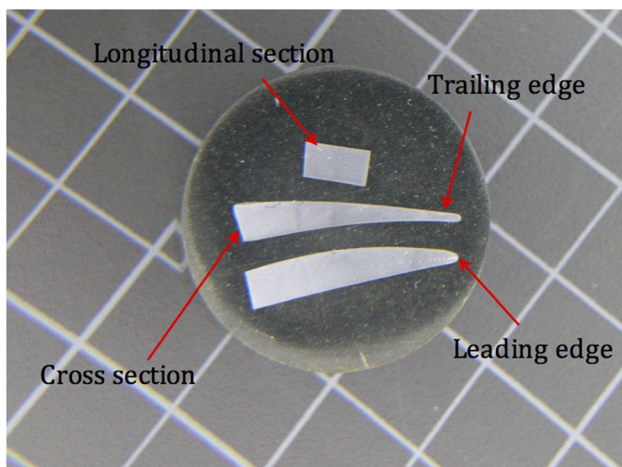


**Fig. 4** Reference blade metallographic sample, cross and longitudinal sections, as per the ASTM E3 standard

mately 305 HV). These results are within range of the values found in the literature [6].

**Microstructure**

*Blade No. 1 (Fractured Blade)*

Figure 5 shows an optical microscope image of the fractured blade. A homogeneous microstructure of tempered martensite is observed, with no preferential orientation, and presence of several carbides.

Figure 6 shows a SEM image of several carbide precipitations on the grain boundaries and inside the grains at the leading edge of the fractured blade.

Additionally, a 60 μm thick surface coating was observed on the same blade. An EDS analysis was performed on this coating. This is shown in Fig. 7a and b. High levels of Aluminum and Magnesium were found because of that analysis.

The structure found on the different zones of the fractured blade did not present any significant morphological variation. This kind of microstructure is characteristic of the forging manufacturing process, followed by a tempering and quenching heat treatment [5, 8, 10]. On the other hand, the coating found in the material is an aluminide coating, which provides a higher corrosion and oxidation resistance [11].

*Blade No. 3*

The microstructure found on blade No. 3 is like the one found on the fractured blade; a matrix without a preferential orientation of tempered martensite with carbides on the grain boundary and inside it is observed. The coating

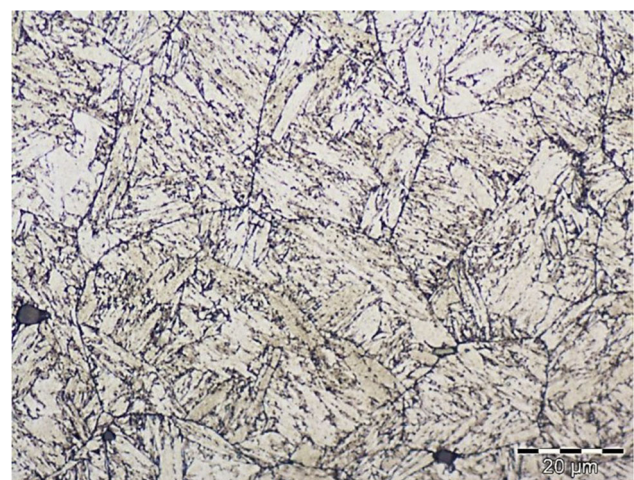


**Fig. 5** Optical microscope image of the trailing edge of the fractured blade at 1000×. Carbides, grain boundaries and tempered martensite are found



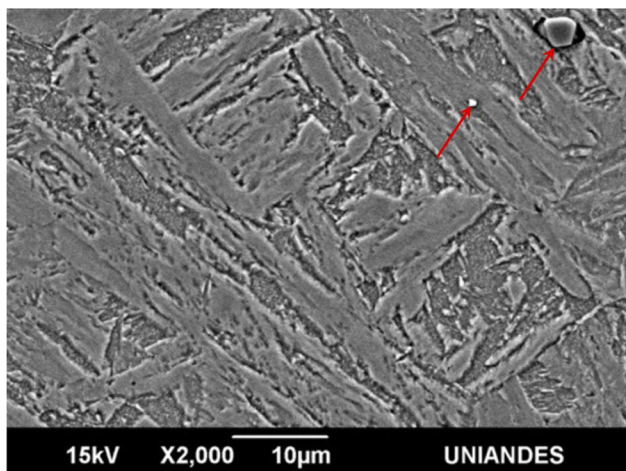


**Fig. 6** SEM image (2000×) of quenched martensitic strips and primary grains at the leading edge of the fractured blade. The arrows indicate some precipitated carbides

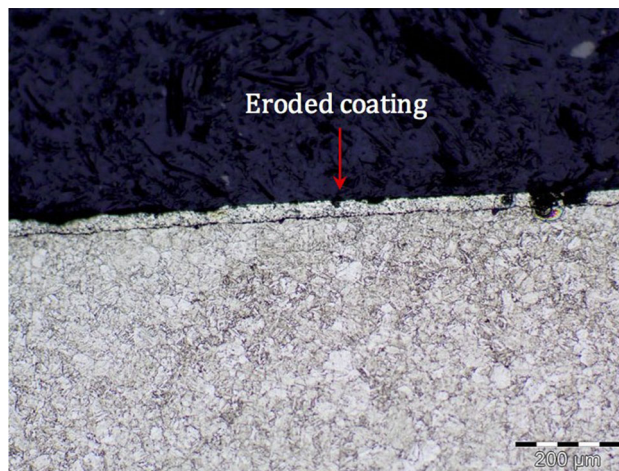
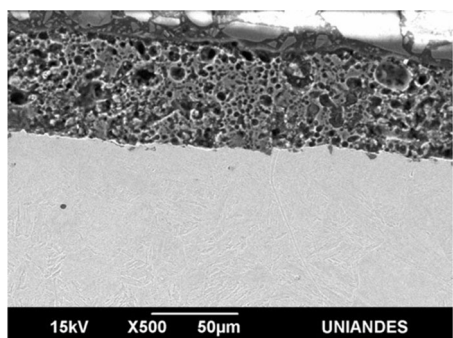
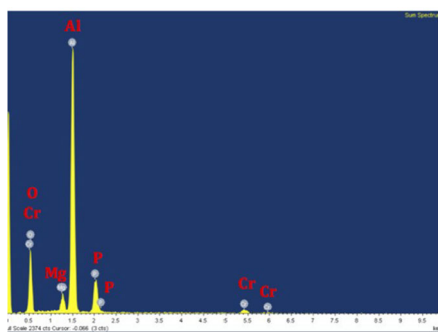


**Fig. 8** Image (100×) of the leading edge of blade No. 3, showing a homogeneous structure and the deposited coating



SEM image (500X) showing a 60 µm thick coating



EDS results of the coating, showing a high concentration of Al and Mg

**Fig. 7** Examination of the coating

presents erosion (Fig. 8), probably due to the engine operation. In most places, the coating thickness is reduced to 30 µm, and it was completely lost in some locations.

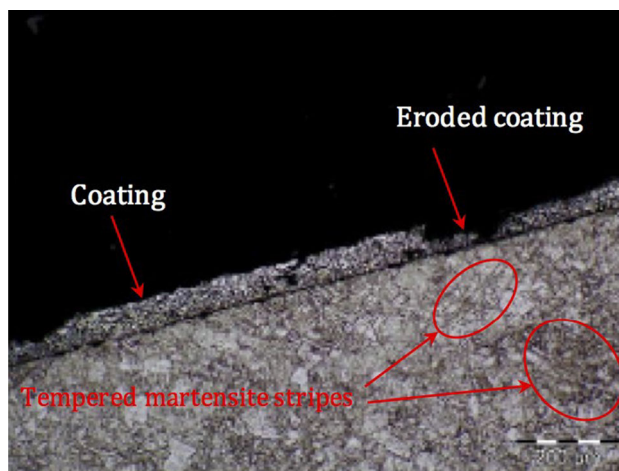


**Fig. 9** Image (100×) of the leading edge of blade No. 26, showing a homogeneous structure of tempered martensite and a coating with eroded sections

*Blade No. 26 and Reference Blade*

The microstructures found on blade No. 26 and on the reference blade are the same and correspond to the one already seen in the previous components. See Figs. 9 and 10. It contains a matrix without orientation of tempered martensite with carbides on the grain boundaries and inside it. The reference blade has a thicker coating, since it has not been exposed to the erosive conditions of the engine operation.

It can be concluded that the microstructural characteristics of all the samples studied are the same. This is a result of using the same manufacturing and coating processes on all blades.

## Failure Analysis

### Fractographic Analysis

A macrography of the failure surface is shown in Fig. 11. By visual examination, it is apparent that the failure surface has two main regions: one in which the presence of beach marks is evident, indicating that fatigue crack propagation took place, and a second one corresponding to the cross section of the material that failed suddenly after the crack grew to a critical length. Above the crack propagation region, a 19x magnified image of the surface is shown. The beach marks are very evident. Also, a 2000x magnified SEM image of the same surface is shown, with some signs of striation. The reduced level of striation is due to the occurrence of ductile tearing, frequently observed with fatigue crack propagation in martensitic steels.

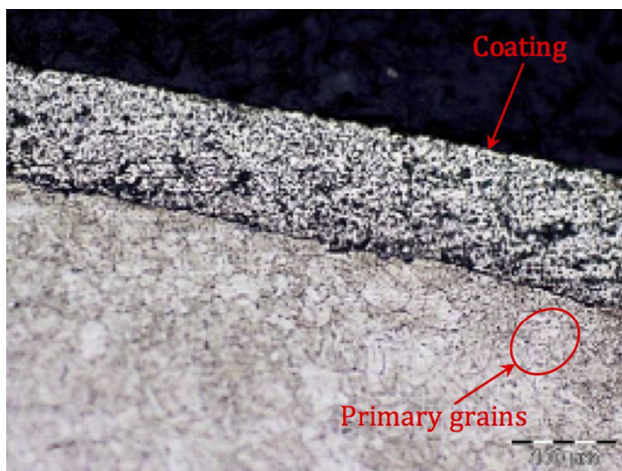
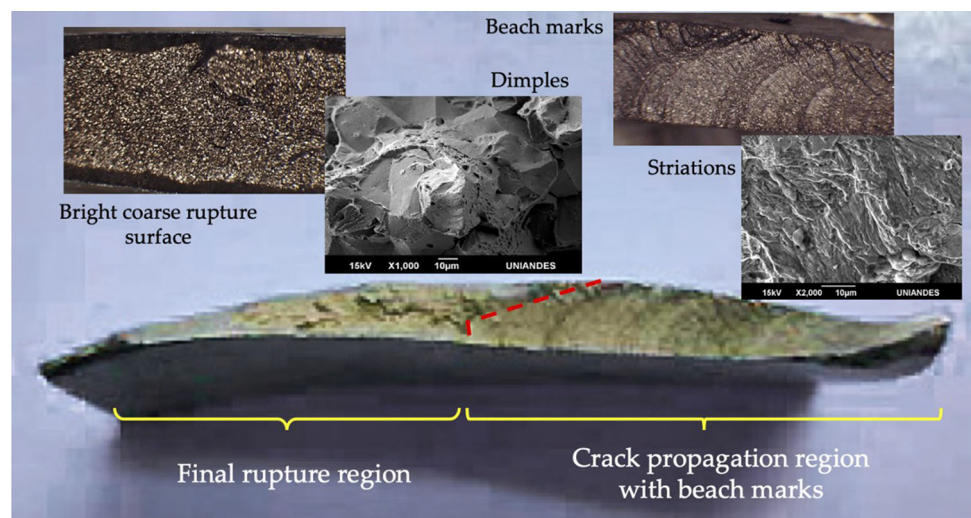


**Fig. 10** Image (200×) of the leading edge of the reference blade, showing some primary grains and a coating with no erosion damage

**Fig. 11** Macrography of the failure surface showing two main regions



Similarly, above the final rupture region, a 19x magnified image of the surface is shown. A coarse and brilliant texture of the surface is evident. A 1000x magnified SEM image of the same surface is shown too, indicating the presence of dimples. These two observations are an indication of intergranular fracture. As shown in Fig. 12, a dent was found on a surface adjacent to the fracture surface, on the pressure side of the blade, next to its leading edge. As shown in Fig. 13, the likely origin of the fatigue beach marks on the fracture surface is

at a location included in the dent.

By visual examination, it was determined that the fracture was produced at approximately 40% of the length of the blade, measured from the dovetail (Fig. 3b). This region is particularly sensitive to any defect due to its proximity to a high vibration section of the blade because of engine operation (between 25 and 35% of the length of the blade) [12].

### Likely Cause of Failure

Examination of the failed component shows that the fracture was originated on the pressure side of the blade, at a border point on the leading edge, where flexure is high due to vibration of the component. A dent is present at that location. This kind of dents is caused on jet engine compressor blades by high-velocity impact of hard debris particles. In the aircraft maintenance industry, it is known as foreign object damage (FOD).

In this section, we consider the hypothesis that foreign object damage (FOD) was the cause for the engine failure. FOD is produced by the high-speed impact of hard debris particles on an internal engine component. This kind of damage typically takes place while the aircraft is in an airfield, with the engine running, and a particle is found



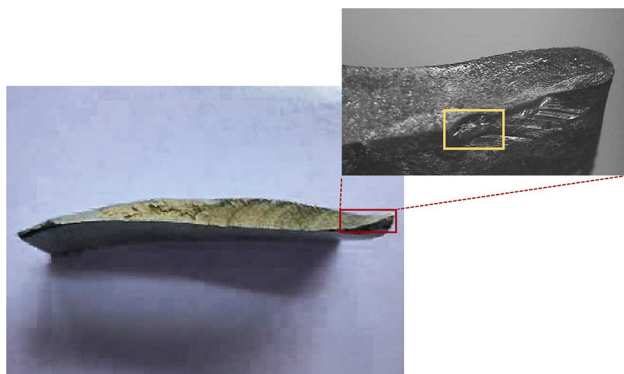


**Fig. 12** Location and magnified view of the dent found on the fractured blade

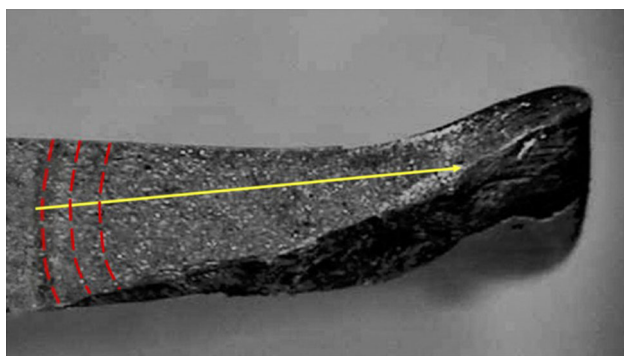


**Fig. 13** Location of the dent with respect to the origin of the beach marks

close enough to the engine so as to be ingested by it. The visible effect of FOD is a notch or a dent on the surface of the component at the point of impact.

Two observations can initially be made in favor of this hypothesis:

The FOD occurred on a blade located on the second stage of the engine compressor. Since the compressor is at the front end of the engine (Fig. 1), its blades are the first components exposed to the incoming air from outside, and therefore the blades on the first stages of the compressor are the ones with the highest risk of being impacted by foreign objects.

The damage took place at a location on the component where it has been observed before with a substantial probability. The impact took place on a point located at 43% of the total length of the blade (Fig. 3b), measured from its root, on the pressure side of the blade, near its leading edge. See Fig. 14. According to [13], for blades located at the second compressor stage, approximately 10% of the FOD impacts are observed at this location. While this is not a very large probability, it is not negligible either and therefore it is good enough to verify the second condition.

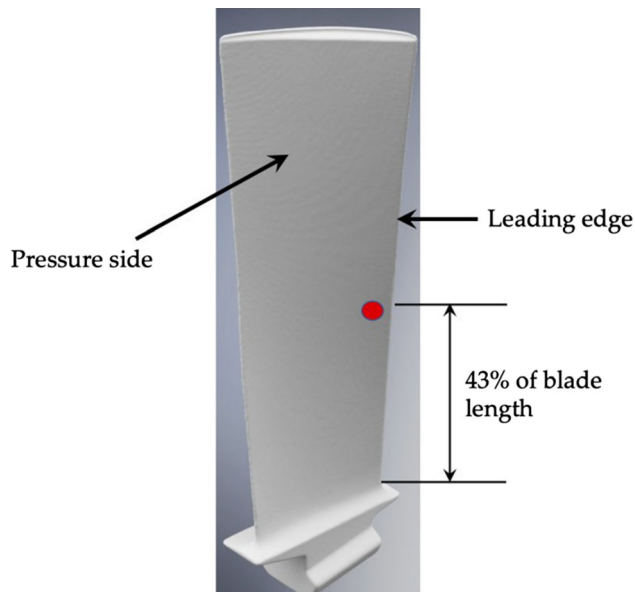


**Fig 14** The red circle indicates the approximate location of the damage on the blade (Color figure online)

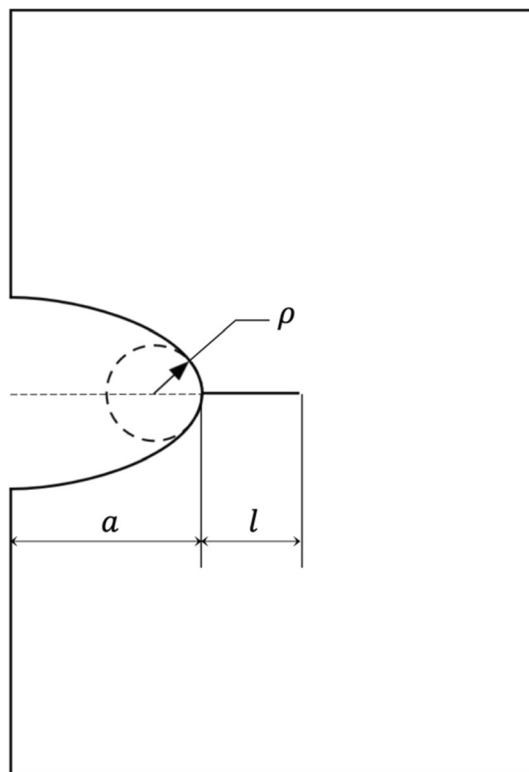


**Fig. 15** Notch with crack geometric model

One important question remains to be answered regarding the FOD hypothesis. The question is whether the stresses induced on the component by FOD were high enough to produce the failure. Answering this question requires the formulation and use of a couple of

mathematical models. The first model is used to establish a failure criterion. This criterion will be based on the calculation of a limit stress level at the FOD location, beyond which failure will occur. The failure mechanism typically associated with FOD is high-cycle fatigue (HCF). The second model is used to determine whether the stress level at the failed blade was likely to have reached a value beyond the limit defined by the failure criterion mentioned above.

Establishment of the Failure Criterion

The model used to establish the failure criterion is the Worst-Case Notch (WCN) model proposed in [13] and [14]. This is a model based on crack-growth theory from fracture mechanics. The model assumes that the lowest threshold stress for the initiation of HCF is determined by whether the growth of micro-cracks can continue after having been initiated earlier by FOD. The WCN model has been experimentally validated, showing good correlation between experimental and predicted data [13, 14].

The goal of the WCN model is to calculate the minimum crack propagation threshold stress as a function of the FOD notch geometry. This calculation is based on a crack propagation model developed for short cracks emanating at the root of a semi-elliptical shaped notch [15]. Such a crack model is shown in Fig. 15, where  $a$  is the notch depth,  $\rho$  is

the notch radius and  $l$  is the crack length. The minimum crack propagation threshold stress is the stress level at which the onset of HCF can occur. It is denoted by  $\Delta S_{th}$  and

$$\Delta S_{th} = \frac{\Delta K_{th}}{k' \sqrt{\pi(l + l_0)}} \tag{Eq 1}$$

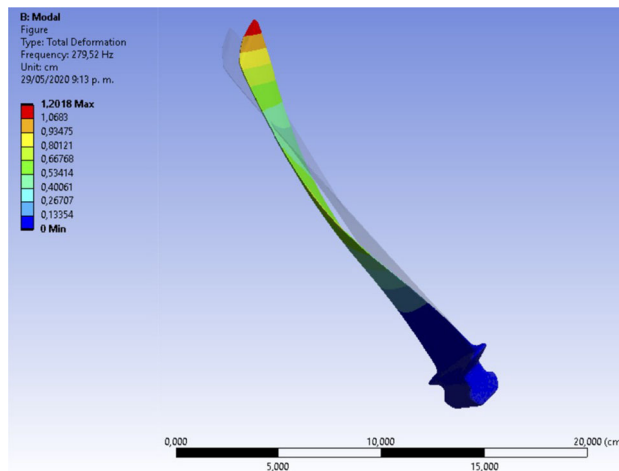
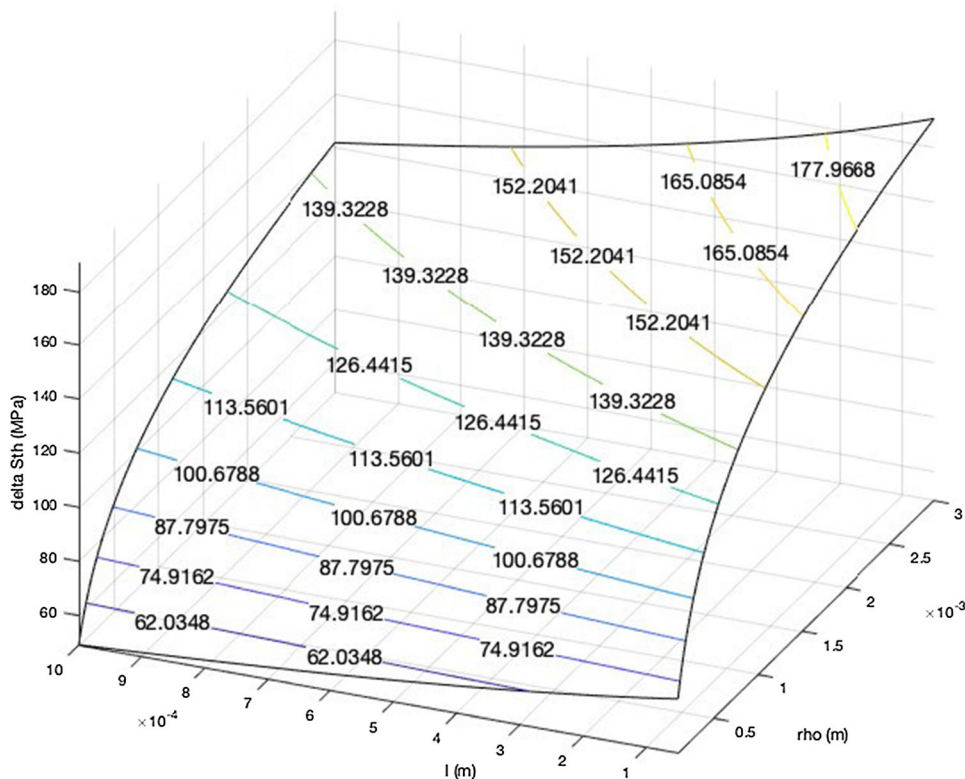


Fig. 17 The first vibration mode of the blade

Fig. 16  $\Delta S_{th}$  as a function of notch bottom radius  $\rho$  and crack length  $l$



where  $\Delta K_{th}$  is the threshold stress intensity factor of the blade material,  $l$  is the crack length,  $l_0$  is a material constant that characterizes the propagation of short cracks vs the propagation of long cracks, and  $k'$  is the elastic stress concentration factor for a crack emanating at the root of a semi-elliptical notch. For AISI 403 steel,  $\Delta K_{th} = 22 \text{ MPa}\sqrt{\text{m}}$  [16].

The expression for  $l_0$  is

$$l_0 = \frac{1}{\pi} \left( \frac{\Delta K_{th}}{\Delta \sigma_e} \right)^2 \quad (\text{Eq 2})$$

In this equation,  $\Delta \sigma_e$  is the nominal fatigue endurance stress range for the material. For AISI 403 steel,  $\Delta \sigma_e = 430 \text{ MPa}$  [16]. The stress concentration factor  $k'$  varies between the maximum and minimum values indicated as follows:

$$k' = 1.12k_t \quad \text{if } l \ll a \quad (\text{Eq 3})$$

$$k' = \sqrt{\frac{l+a+l_0}{l+l_0}} \quad (\text{Eq 4})$$

In this equation,  $k_t$  is the elastic stress concentration factor for the notch without the crack.  $k_t$  is given by

$$k_t = \frac{1 + 2.48/\sqrt{\epsilon} + 1.16/\epsilon}{1 + 0.517/\sqrt{\epsilon}} \quad (\text{Eq 5})$$

where  $\epsilon = \rho/a$  [17].

At this point, we are ready to compute  $\Delta S_{th}$  from Eq. 1, for a range of notch radii  $\rho$  and crack lengths  $l$ . The notch depth  $a$  is fixed at 0.65 mm, which was measured on the failed blade sample. The chosen ranges, in mm, are  $0.1 \leq \rho \leq 3.0$  and  $0.05 \leq l \leq 1.0$ . The result is shown in Fig. 16. As expected,  $\Delta S_{th}$  increases as  $\rho$  increases and decreases as  $l$  increases.

According to the WCN model, for each pair of values  $\rho$  and  $l$ , any stress at the notch location that is above  $\Delta S_{th}$  will cause failure by crack propagation. For the chosen values of  $a$ ,  $\rho$  and  $l$ , the value of  $\Delta S_{th}$  ranges between 54 MPa and 180 MPa.

#### Determination of the Stress Level at the Notch Location

At this point, we determine the stress level at the FOD notch. To that end, we use a finite elements model of the blade. The crack propagation was caused by bending stress variations due to the vibrations of the blade during the engine operation. For this reason, we use finite elements to model the vibrations of the blade, looking for the bending stresses and total deformations induced by those vibrations. The model was built and run in the ANSYS Workbench R19 system. A modal analysis was performed first. This model included the tension stress induced on the blade by the centrifugal force caused by the rotation of the engine.

This force is very significant, since the rotation speed of this engine can be as high as 8000 rpm. The only boundary condition defined for this analysis was a fixed support at the root of the blade, representing the way in which it is assembled in the compressor rotor.

Although in the modal analysis we calculated the first five natural frequencies and vibration modes of the blade, the most important is the first one, since in this mode the blade will present the largest deformations and the largest stresses. The first natural frequency was at 279.52 Hz. The first vibration mode is shown in Fig. 17. In the figure, the absolute value of the deformations shown is not important.

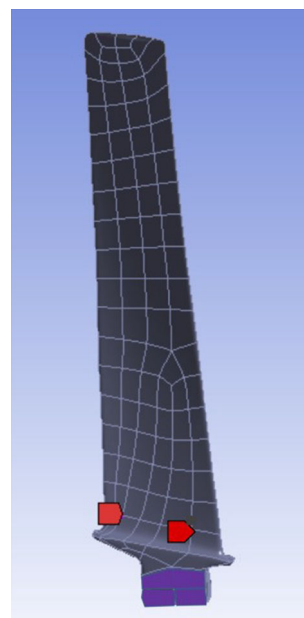


**Fig. 18** Boundary conditions for the harmonic response analysis

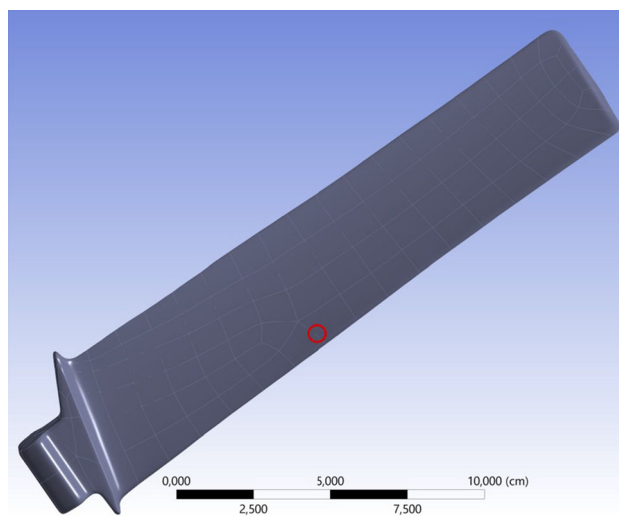


**Fig. 19** Location of the FOD



**Fig. 20** Stress distribution with 180 MPa at the FOD location

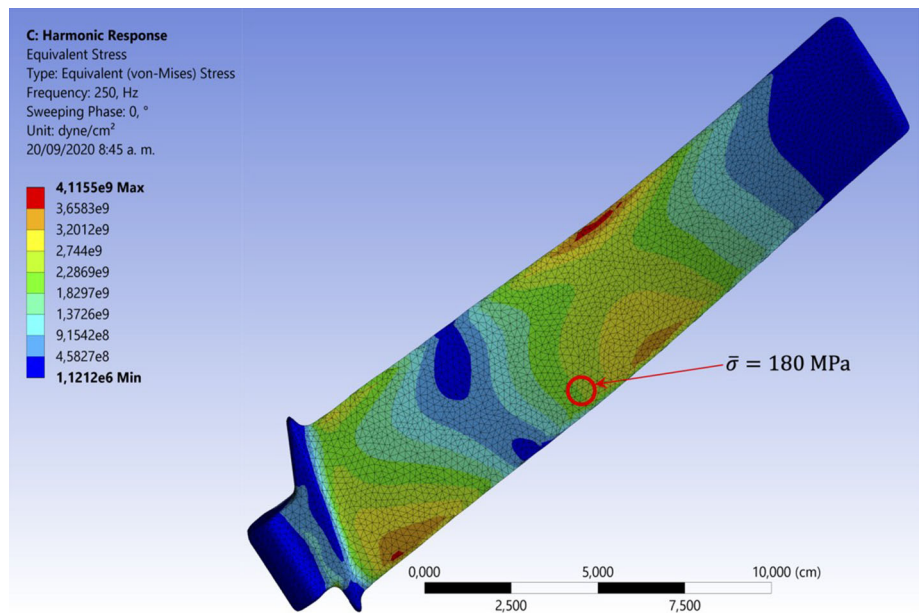
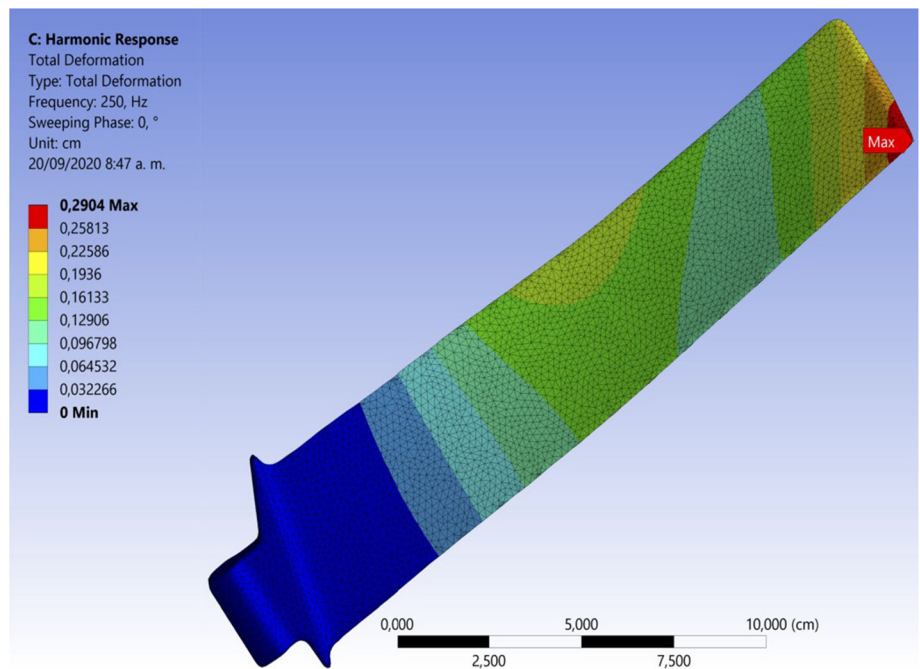


**Fig. 21** Vibration amplitude associated with a stress of 180 MPa at the FOD location



The relative deformations between any two points in the blade are the important result, since they describe the general shape that the blade will have while vibrating in that mode. As expected, in that case the blade deflection

will be like the one observed if a force perpendicular to the blade was applied at its free end.

With the results of the modal analysis, a harmonic response analysis was performed on the blade. The

boundary conditions of that analysis are shown in Fig. 18. The purple surfaces are completely immobilized, as well as the ones directly on the opposite side of the blade. An oscillating force is applied perpendicular to the surface of the blade along the line between the two vertices with a red flag. The force is applied at a frequency of 250 Hz, so that it will excite primarily the first vibration mode of the blade.

The foreign object impact occurred approximately at the location highlighted with a circle in Fig. 19. Having identified the failure location in the mesh, we will use the finite elements model of the harmonic response to determine the amplitude of the vibration needed to produce the threshold stresses predicted with Equation 1 in the range between 54 MPa and 180 MPa. The result is that to obtain a stress of 54 MPa at the FOD location, the vibration amplitude must be 0.52 mm, and to obtain a stress of 180 MPa at the same location, the vibration amplitude must be 2.90 mm. Figure 20 shows the stress distribution in the blade surface such that at the FOD location the average stress is 180 MPa. On the other hand, Fig. 21 shows the vibration amplitude observed when the stress at the FOD location is 180 MPa.

These blade tip deflections are well within the level of blade deflection reported in the literature [12] as caused by vibration under normal operation of the engine. This is an important result since it answers affirmatively the question on whether the stress level at the FOD location is high enough to cause fatigue failure of the blade. With this result and the two observations made at the beginning of this section on the FOD hypothesis, it can be said that, although it cannot be said with total certainty that FOD caused the failure of the blade, it cannot be ruled out either.

## Conclusions

The presence of beach marks over the fractured surface of the failed blade with origin on the pressure side of the blade indicates that a fatigue mechanism was responsible for the crack propagation. The close separation of the striation on the fractured surface is a result of ductile tearing and a low stress fatigue mechanism. The fibrous and brilliant region with dimples at the center of the blade corresponds to an intergranular fracture, which could be generated by the precipitation of carbides on the grain boundaries.

FOD due to high-speed impact of a particle on the compressor blade surface cannot be ruled out as a possible cause of the failure. The failure criterion produced by the WCN model and the calculation of the associated maximum allowable blade tip deflections indicate that they correspond to levels commonly found during normal engine operation. To mitigate the risk associated with this

cause of failure, it is recommended to put into practice a very rigorous non-destructive inspection program. The use of radiography, ultrasonic or dye penetrant techniques is suggested.

## References

1. V. Infante, J.M. Silva, M. de Freitas, L. Reis, Failure analysis of compressor blades of aeroengines due to service. *Eng. Fail. Anal.* **16**, 1118–1225 (2009)
2. L.M. Amoo, On the design and structural analysis of jet engine fan blade structures. *Prog. Aerosp. Sci.* **60**, 1–11 (2013)
3. X. Chen, Foreign object damage on the leading edge of a thin blade. *Eng. Fail. Anal.* **37**, 447–457 (2005)
4. ASTM International, West Conshohocken, PA, ASTM E1282. *Standard guide for specifying the chemical compositions and selecting sampling practices and quantitative analysis methods for metals, Ores and Related Materials* (ASTM International, 2012)
5. J.R. Davis, *Stainless Steels* (ASM International, Almere, 1994)
6. S. Kyo-Soo, K. Seon-Gab, H. Young-Ha, Failure of a J79 engine compressor blade due to stall. *J. Fail. Anal. Prev.* **7**, 212–217 (2007)
7. ASTM E18-08b, *Standard Test methods for rockwell hardness of metallic materials* (ASTM International, 2008)
8. H.E. Chandler, *Heat treater's guide: practices and procedures for irons and steels* (ASM International, 1995)
9. ASTM E384-11, *Standard Test method for microindentation hardness of materials* (ASTM International, 2011)
10. *ASM Handbook*, vol 1. 10th edn. (ASM International, 1990)
11. F.J. Bolivar, L. Sánchez, F.J.P.M.P. Hierro, Aluminización de aceros ferríticos-martensíticos (HCM-12A) mediante CVD-FBR. *Scientia et Technica.* **13**(36), 619–624 (2007)
12. J.A. Kaufman, A.J. Meyer, *Investigation of the effect of impact damage on fatigue strength of jet-engine compressor rotor blades, Technical report.* (National Advisory Committee for Aeronautics (NACA), Cleveland, 1956)
13. J. Gallagher, R. vanStone, R. deLaneuville, P. Gravett, R. Bellows, D. Slavik, S. Hudak, T. Duniyak, A. Berens, T. Farris, K. Chan, R. Mc-Clung, C. Annis, D. Corbly, A. Grandt, D. Anton, P. Kurath, J. Sheldon, C. Weeks, Y. Lenets, B.H. Lawless, J. Ruschau, *AFRL-ML-WP-TR- 2001- 4159. Improved High-Cycle Fatigue (HCF) Life Prediction.* Technical report AFRL-ML-WP-TR-2001-4159 (University of Dayton Research Institute. Materials and Manufacturing Directorate. Air Force Research Laboratory, 1999)
14. TR-AVT-094. Best practices for the mitigation and control of foreign object damage-induced high cycle fatigue in gas turbine engine compression system airfoils, RTO Technical Report, North Atlantic Treaty Organisation (NATO). Research and Technology Organisation (2004)
15. K.S.M. El-Haddad, T. Topper, Prediction of non-propagating cracks. *Eng. Fract. Mech.* **11**, 573–584 (1979)
16. W.A. Logsdon, An Evaluation of the crack growth and fracture properties of AISI 403 modified 12 Cr stainless steel. *Eng. Fract. Mech.* **7**, 23–40 (1975)
17. A.K.M.P. Savruk, *Stress concentration at notches.* (Springer International Publishing, New York, 2017)

**Publisher's Note** Springer Nature remains neutral with regard to jurisdictional claims in published maps and institutional affiliations.